

SIR: Self-supervised Image Rectification via Seeing the Same Scene from Multiple Different Lenses

Jinlong Fan

Jing Zhang

Dacheng Tao

UBTECH Sydney AI Centre, Faculty of Engineering, The University of Sydney

Abstract

Deep learning has demonstrated its power in image rectification by leveraging the representation capacity of deep neural networks via supervised training based on a large-scale synthetic dataset. However, the model may overfit the synthetic images and generalize not well on real-world fisheye images due to the limited universality of a specific distortion model and the lack of explicitly modeling the distortion and rectification process. In this paper, we propose a novel self-supervised image rectification (SIR) method based on an important insight that the rectified results of distorted images of the same scene from different lenses should be the same. Specifically, we devise a new network architecture with a shared encoder and several prediction heads, each of which predicts the distortion parameter of a specific distortion model. We further leverage a differentiable warping module to generate the rectified images and re-distorted images from the distortion parameters and exploit the intra- and inter-model consistency between them during training, thereby leading to a self-supervised learning scheme without the need for ground-truth distortion parameters or normal images. Experiments on synthetic dataset and real-world fisheye images demonstrate that our method achieves comparable or even better performance than the supervised baseline method and representative state-of-the-art methods. Self-supervised learning also improves the universality of distortion models while keeping their self-consistency.

1. Introduction

Wide field-of-view (FOV) cameras can capture wide-angle images that record more contents than conventional normal ones at a single shot, making them useful in many vision tasks [24, 2, 28, 8]. However, the wide FOV lenses break the pinhole camera assumption, introducing distortion in the images. To facilitate downstream applications and leverage the off-the-shelf models trained on nor-

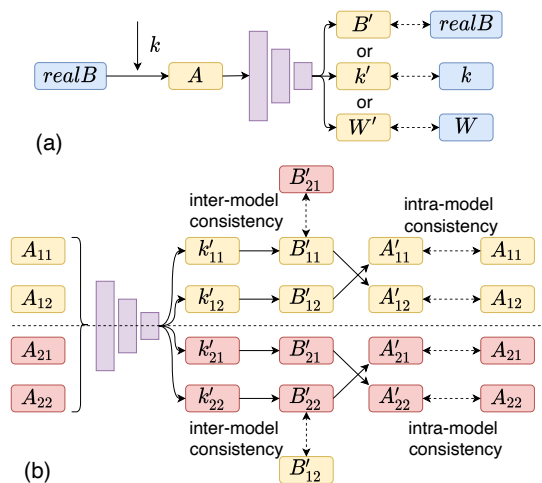


Figure 1. (a) Deep supervised methods predict the distortion parameters k' , warping field W' , or the rectified image B' from the distorted image A , which is synthesized from the normal image $realB$ based on a sampled parameter k of a specific distortion model. The loss is calculated between the prediction and its ground truth, e.g., k and k' . (b) Our SIR is a deep self-supervised method without the need for any annotations. It uses the intra- and inter-model loss for training, where the former calculates the re-projection loss between the re-distorted images A' from the same distortion model but with different parameters (marked by the same color) and the latter calculates the re-projection loss between the rectified images B' from different models.

mal images, image rectification is often used as the pre-processing step to correct the distortions. Various traditional geometry-based methods have been proposed in the past decades which formulate image rectification as an optimization problem [5, 1, 41, 27]. Recently, deep learning-based methods have shown promising results by leveraging the representation power of deep neural networks [29, 40, 20, 21, 38, 39]. Nevertheless, how to improve the universality of deep models that can rectify images of different distortion types and generalize well on real fisheye images remains challenging.

Since real-world paired wide-angle and normal images are difficult to collect and no annotations of the distortion model are available, existing deep learning methods usually use synthetic datasets for training [29, 4, 30]. Wide-angle images are synthesized based on normal ones from a base dataset, *e.g.*, ADE20k [42], where a specific distortion model is used and distortion parameters are uniformly sampled from a pre-defined range. Based on the synthetic datasets, most deep learning-based methods adopt a supervised learning scheme that the network is trained to predict the distortion parameters, the equivalent warping field, or the rectified image from the distorted image as shown in Figure 1(a). However, it is difficult to discover visual clues and learn representative features for predicting distortion parameters directly from the distorted images [23]. To address this issue, extra annotations have been used to help the prediction. For instance, Yin *et al.* [40] used scene parsing information to guide the training while Xue *et al.* [38] leverages annotations of straight lines to constrain the predicted distortion parameter. However, the annotations of semantic masks or geometry structures are difficult and laborious to obtain. Besides, specific network architectures or losses should be carefully devised to leverage those annotations, which may also introduce extra complexity.

The other problem is that since the training dataset is synthesized using a specific distortion model, the rectification ability of the trained network is bound with that model. It may have a good *self-consistency* but with a bad *universality*, where the former refers to the ability to rectify images with the same types of distortions while the latter refers to the ability to generalize well on images from other distortion models or real-world fisheye images from different lenses [35]. Recently, some methods have been proposed to predict warping fields instead of parameters, which can represent multiple distortion models in a single framework [20, 22]. The networks are trained by leveraging the supervisory signals from all the ground-truth warping field derived from different distortion models and distortion parameters. For example, Li *et al.* [20] used six types of distortions to generate the synthesized dataset while Liao *et al.* [22] increased the number to sixteen. However, it is difficult to regress the warping fields directly from the distorted images. Moreover, mixing all training images from different distortion models makes it hard to leverage their complementary and consistency explicitly, thereby leading to a compromised model with limited generalization.

In this paper, we propose a Self-supervised Image Rectification method (SIR) based on the insight that the rectified results of distorted images of the same scene from different lens should be the same. Specifically, for the distorted images from the same distortion model but with different parameters or from different distortion models (*i.e.*, different lenses), their rectified images should be the same,

i.e., *intra-model consistency* in the former case and *inter-model consistency* in the latter case. To exploit such consistency for image rectification, we devise a new network architecture with a shared encoder and several prediction heads, each of which predicts the distortion parameter of a specific distortion model. As shown in Figure 1(b), the rectified images are further re-distorted by using the predicted parameters from its counterpart (marked in the same color). Then, we use a re-projection loss to calculate the difference between the input distorted image and re-distorted one (*e.g.*, A'_{11} and A_{11}) to keep intra-model consistency. Moreover, we add an inter-model consistency constraint on the rectified image from different distortion models (*e.g.*, B'_{21} and B_{11}). In this way, SIR exploits the complementary and consistency between different distortion models and is trained in a self-supervised manner without the need for ground-truth distortion parameters or normal images.

The contribution of this paper is threefold:

- We propose a novel self-supervised learning method for image rectification without the need for paired training data or any annotations.
- We devise two novel intra- and inter-model consistency losses to leverage the complementary and consistency between different distortion models via a differentiable forward and backward warping module.
- Experiments on both synthetic datasets and real-world fisheye images demonstrate that our method can achieve comparable or better rectification and generalization performance than representative methods.

2. Related Work

Image Rectification. Traditional methods formulate image rectification as an optimization problem, where the objective function can be some energy and/or loss terms that measure the distortions in the image. For instance, lines are one of the most widely used visual cues since the curved lines due to distortion should be straight after rectification [25, 41]. Recently, some visual attention-based methods have also been proposed for image rectification [7, 37, 31], which emphasize to preserve the shape of semantic content such as faces in portraits or buildings in the scene. The attention map could be determined interactively by users or automatically by algorithms [7, 18]. Although attention map can provide informative guidance for predicting local-adaptive warping field and obtaining the better perceptual result, the optimization process is usually difficult and unstable. When multi-view images from the same lens are available, multi-view geometry constraints can also be leveraged to estimate accurate and robust distortion parameters, such as the epipolar constraint of points correspondence [13, 33, 19, 3, 32]. Our method shares some merits

with the multi-view method but with significant differences. First, it also uses multiple images but only for training and the images are captured at the same viewpoint by different lenses (*e.g.*, different distortion models or parameters). Second, since the distorted images in our setting share the same intermediate rectified images, dense point correspondence can be constructed via an efficient differentiable forward and backward warping module and reprojection loss is used for training, instead of sparse point correspondence and epipolar constraint-based loss in multi-view methods.

In contrast to traditional geometry-based methods which are error-prone and time-consuming due to separate stages (*e.g.*, for line detection and rectification) and iterative optimization, efficient deep learning-based methods have attracted increasing attention recently, which can be categorized into model-based methods [29, 40, 4, 30, 23, 38] and model-free methods [20, 21, 22]. Model-based methods directly regress the distortion parameter of a specific distortion model from the input distorted image. Their performance is limited by the universality of the specific distortion model. By contrast, model-free methods estimate the warping field that is used to warp the distorted image to an undistorted one or generate the rectified image directly. They can incorporate multiple models in one framework [20, 22]. Both kinds of methods need labels for supervised training, *e.g.*, the distortion parameters, warping fields, or normal images. Our method falls into the model-based group but is a self-supervised one, which can be trained with unlabeled data. Moreover, it leverages the “multi-view” consistency between different distortion models with different distortion parameters, thereby improving the generalization.

Self-supervised Learning. As a sub-area of unsupervised learning, self-supervised learning has been a hot research topic recently [16, 26, 17]. It aims to learn a useful feature representation for downstream tasks by solving the pretext tasks. The pretext tasks can be constructed based on spatial/temporal context, semantic labels, multi-modal correspondence, etc. For example, SimCLR defines a context-based contrasting task for self-supervised learning [10], which obtains a comparable performance as fully supervised models. Recently, Chao *et al.* [9] introduced self-supervised learning into image rectification, which assumes the distortion is radial-symmetric, *i.e.*, when an image is rotated or flipped w.r.t. the center, the warping field of the distorted image should keep the same. Thereby, they exploit such consistency to train their model in a self-supervised manner. By contrast, we exploit the consistency between the rectified and re-distorted images of distorted images from different distortion models, *i.e.*, the intra-model consistency and the inter-model consistency. Our method is model-based and explicitly model the distortion and rectification process via an efficient differentiable forward and backward warping module, which is easy to train.

3. Self-supervised Image Rectification

3.1. Network Architecture

Our self-supervised image rectification neural network has a shared encoder implemented by the ResNet-50 [14], multiple prediction heads (*e.g.*, three heads in this paper), and a differentiable forward and backward warping module attached to each head as illustrated in Figure 2.

Shared Encoder. In this paper, we adopt ResNet-50 as the share encoder, which embeds an input distorted image of size $257 \times 257 \times 3$ into a feature vector of size $1 \times 1 \times 2048$. During training, it is fed of a batch of grouped distorted images, where each group of distorted images are synthesized from a same normal image from a base dataset according to different distortion models. Specifically, we randomly sample two different distortion parameters from a pre-defined uniform distribution for each distortion model and synthesize two distorted images accordingly. Although there is no limit of the number of distortion models used in our method, we choose three typical ones in this paper, *i.e.*, the **FOV** distortion model (denoting “FOV”) [36], one parameter **D**ivision **M**odel (denoting “DM”) [13], and **E**qui**D**istant distortion model (denoting “ED”) [15]. Each of them has a single parameter and an analytical forward (distorted→normal) and backward (normal→distorted) warping function. Thereby, each group has six distorted images, *i.e.*, $\{A_i^j | i \in \mathcal{M}; j = 1, 2\}$, $\mathcal{M} = \{FOV, DM, ED\}$.

Prediction Head. We attach three prediction heads to the shared encoder (*i.e.*, h_{FOV} , h_{DM} , and h_{ED} in Figure 2), each of which corresponds to a specific distortion model since their distortion parameters have different meanings and value ranges. We use a fully connected layer for each head, which has a single output neuron that outputs the predicted parameter, *i.e.*, K_{FOV} , K_{DM} , and K_{ED} in Figure 2. Note that since the network inputs are $\{A_i^j | i \in \mathcal{M}; j = 1, 2\}$, their encoded features are further split and fed into the corresponding prediction head, where each pair of parameters can be predicted as shown in Figure 2. They correspond to the distorted images that are generated by the same distortion model as the one modeled by the prediction head. Since the magnitude of the parameters from different distortion models differs significantly, we normalized the parameter to the range of $[0, 1]$ and used a Sigmoid activation function after the prediction head. Specifically, assuming the minimum and maximum value of the parameter for a distortion model is k_{min} and k_{max} , the parameter k is normalized as follows:

$$k = (k - k_{min}) / (k_{max} - k_{min}). \quad (1)$$

Warping Module. Given the predicted distortion parameter, we can get the rectified normal image using the forward warping function, which describes the mapping re-

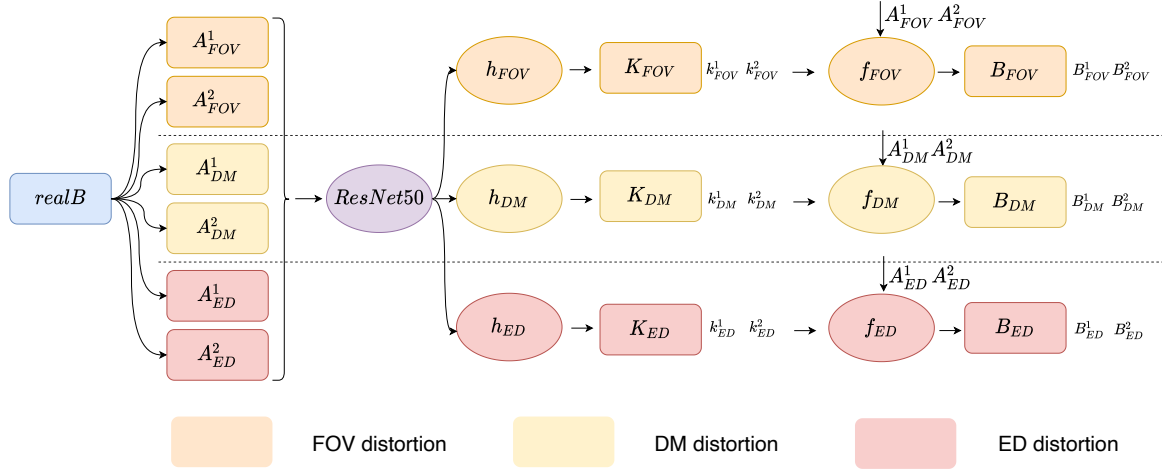


Figure 2. Diagram of the architecture of SIR. During training, three pairs of distorted images are synthesized from the same normal image $realB$ using three distortion models, *i.e.*, FOV, DM, and ED. The images in each pair (*e.g.*, A_{FOV}^1 and A_{FOV}^2) are synthesized using different distortion parameters. A batch of these paired data is fed into a shared encoder implemented by the ResNet-50. Three prediction heads (*e.g.*, h_{FOV}) are then used to predict the distortion parameters, *e.g.*, k_{FOV}^1 and k_{FOV}^2 , where each head corresponds to a specific distortion model. Then, a forward warping module (*e.g.*, f_{FOV}) is used to generate the rectified images, *e.g.*, B_{FOV}^1 and B_{FOV}^2 .

relationship between corresponding pixels from the distorted image to the normal image. Conversely, given the normal image and distortion parameter, we can get the distorted image using the backward warping function. Mathematically,

$$B_i^j = f_i(A_i^j, k_i^j), \quad (2)$$

$$\hat{A}_i^m = f_i^{-1}(B_i^j, k_i^m), \quad (3)$$

where $i \in \mathcal{M}$, $j \in \{1, 2\}$, $m \in \{1, 2\}$, $f_i(\cdot)$ and $f_i^{-1}(\cdot)$ represents the forward and backward warping function, respectively. B_i^j is the rectified image from A_i^j and \hat{A}_i^j is the re-distorted image from B_i^j . When $j \neq m$, Eq. (3) can be used to generate a distorted image from non-paired rectified image and distortion parameter. It will be used for measure intra-model consistency, which will be detailed later. If $f_i(\cdot)$ and $f_i^{-1}(\cdot)$ have an analytical form, we can devise a differentiable neural module to implement it, *i.e.*, using the “grid_sample” function in PyTorch. In this way, we can explicitly model the rectification and distortion process and implicitly set up the dense point correspondence between distorted image and normal image.

For the three models we selected, FOV and DM describe the pixel correspondence using the radial distance r_u in the normal image and the radial distance r_d in the distorted image, while ED sets up the pixel correspondence based on r_d and the angle θ of the incident ray for each point in the distorted image. Specifically, for FOV, we have:

$$r_u = f_{FOV}(r_d, k) = \frac{\tan(kr_d)}{2 \tan(\frac{k}{2})}, \quad (4)$$

$$r_d = f_{FOV}^{-1}(r_u, k) = \frac{1}{k} \arctan(2r_u \tan(\frac{k}{2})), \quad (5)$$

where $r_d = \sqrt{u_d^2 + v_d^2}$, (u_d, v_d) is the coordinate of a pixel on the distorted image. r_u is calculated likewise. Given the pixel coordinate and distortion parameter k , we can obtain the coordinate of its corresponding pixel on the normal image according to Eq. (4), and vice versa according to Eq. (5). Thereby, we can implement them with the “grid_sample” layer in PyTorch, which is differentiable.

Compared with FOV, DM can represent relatively large distortion with fewer parameters, which has also been used widely [1, 29, 30]. In this paper, we only use one parameter for a trade-off between complexity and accuracy. The forward warping function of DM can be written as follows,

$$r_u = f_{DM}(r_d, k) = \frac{r_d}{1 + kr_d^2}. \quad (6)$$

However, the backward warping function is not trivial since we can have two solutions from Eq. 6, *i.e.*,

$$r_d = f_{DM}^{-1}(r_u, k) = \frac{1 \pm \sqrt{1 - 4kr_u^2}}{2kr_u} \quad (7)$$

We choose the smaller positive value as the right solution for sampling nearby pixels. For the ED model, the forward and backward warping function can be written as:

$$r_u = f_{ED}(\theta, k) = k \tan \theta = k \tan(\frac{r_d}{k}), \quad (8)$$

$$r_d = f_{ED}^{-1}(\theta, k) = k \theta = k \arctan(\frac{r_u}{k}). \quad (9)$$

More details about the aforementioned distortion models and other distortion models can be found in [34, 36].

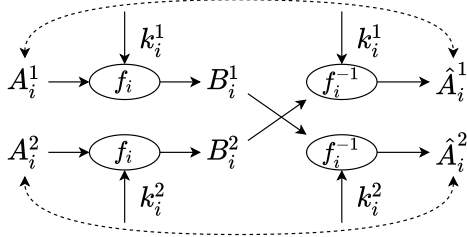


Figure 3. Illustration of intra-model consistency. Given two distorted images A_i^1, A_i^2 synthesized using a same distortion model $i \in \mathcal{M}$ but different parameters k_i^1, k_i^2 , the rectified images B_i^1, B_i^2 can be obtained by forward warping module f_i . Since B_i^1 and B_i^2 should be the same as the underlying normal image, thereby their re-distorted images should be the same with the corresponding input distorted images as long as they share the same distortion parameter, e.g., $A_i^1 = \hat{A}_i^1$ and $A_i^2 = \hat{A}_i^2$.

3.2. Self-supervised Learning

Intra-model Consistency. The intra-model consistency refers to the re-distorted images from a rectified image should be same with the corresponding input distorted images as long as they share the same distortion parameter. It is reasonable since the distorted image is uniquely determined by the parameter for one distortion model. As shown in Figure 3, we re-distort the rectified image (e.g., B_i^1) with the different distortion parameter in the pair (e.g., k_i^2) rather than the distortion parameter (e.g., k_i^1) used for synthesizing the original input distorted image (A_i^1). In the latter case, we may obtain a trivial solution, e.g., when the prediction $k_i^1 = k_i^2 = 0$ in DM, thereby $A_i^1 = B_i^1 = \hat{A}_i^1$. By contrast, in the former case, if $k_i^1 = k_i^2 = 0$ in DM, $A_i^1 = B_i^1 = \hat{A}_i^2 \neq A_i^2$, there will be a significant difference between \hat{A}_i^2 and A_i^2 , which can be used as a loss to supervise the network. Mathematically, the intra-model consistency loss can be calculated as the following L1 loss:

$$L_{intra} = \sum_{i \in \mathcal{M}} \sum_{j=1}^2 |A_i^j - \hat{A}_i^j|. \quad (10)$$

Inter-model Consistency. The inter-model consistency refers to that the rectified images of distorted images from different distortion models should be the same as long as they are synthesized from the same normal image. As shown in Figure 4, A_{DM}^j and A_{ED}^j are two distorted images from the distortion model DM and ED with parameter k_{DM}^j and k_{ED}^j , respectively. Since they are synthesized from the same normal image $realB$, thereby their rectified images should be the same, i.e., $B_{DM}^j = B_{ED}^j = realB$. Mathematically, the inter-model consistency loss can be calculated as:

$$L_{intra} = \sum_{(i,m) \in \hat{\mathcal{M}}} \sum_{j=1}^2 |B_i^j - B_m^j|. \quad (11)$$

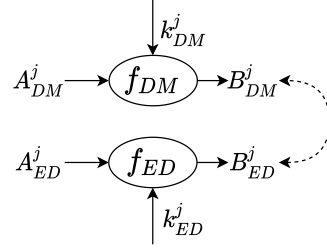


Figure 4. Illustration of inter-model consistency. Given two distorted images A_{DM}^j and A_{ED}^j synthesized from the same normal image using different distortion models and parameters k_{DM}^j and k_{ED}^j , their rectified images should be same, i.e., $B_{DM}^j = B_{ED}^j$.

$\hat{\mathcal{M}} = \hat{\mathcal{M}}_1 = \{(FOV, DM), (FOV, ED), (DM, ED)\}$, or $\hat{\mathcal{M}} = \hat{\mathcal{M}}_2 = \{(FOV, DM)\}$, or $\hat{\mathcal{M}} = \hat{\mathcal{M}}_3 = \{(FOV, ED)\}$, or $\hat{\mathcal{M}} = \hat{\mathcal{M}}_4 = \{(DM, ED)\}$, denoting unordered combinations of all distortion models or any two models. We will present their results in the ablation study.

Training Objective. For self-supervised learning, the final training objective is defined as:

$$L_{total} = L_{intra} + L_{inter}. \quad (12)$$

It is noteworthy that L_{inter} cannot be used alone. Otherwise, it may lead to a trivial solution similar to what we have analyzed in the case of intra-model consistency.

4. Experiments

4.1. Experiment Setting

Dataset and Metrics. We synthesized the training images using the normal images from the ADE20K training set [42]. Three distortion models were used in our experiments, i.e., FOV, DM, and ED. ADE20K dataset contains 20k images for training and 2k images for testing. We synthesized the test set for each distortion model separately. Each normal image was center-cropped with the maximum size at the height or width side and then resized to 257×257 . In the warping module, the image coordinate was normalized to $[-1, 1]$. The distortion parameter of each distortion model was sampled from a uniform distribution within a pre-defined range, i.e., $[-0.02, -1]$ for DM, $[0.2, 1.2]$ for FOV, and $[0.7, 2]$ for ED, which is determined according to two empirical rules. First, the distortions should not be too large such that the valid area in the distorted image would be too small. Second, distortions from different models should be comparable since we need to exploit the inter-model consistency to rectify them into the same normal image. For evaluation metrics, we adopt PSNR and SSIM which have been widely used in prior arts [6, 1, 29, 40, 38]. They can measure the difference between the rectified image and the ground-truth normal one.

Implementation Detail. Although other backbone networks can also be used in the shared encoder, we used ResNet50 as an example in the experiment. For each mini-batch, we used 8 normal images to synthesize the distorted samples, *i.e.*, 48 in total. We used Adam optimizer to train the network for 10 epochs on a single NVIDIA Tesla V100 GPU. The learning rate was set to 0.0001. ResNet50 was initialized using the weights pre-trained on ImageNet [11]. We implemented our network using PyTorch¹. More details and results can be found in the supplementary material.

4.2. Ablation Studies

Learning Paradigm. In order to verify the effectiveness of our self-supervised method, we set up a supervised learning baseline (denoting “SL”) and two self-supervised variants of our SIR model (denoting “SSL-S” and “SSL-M”). SL uses the ground-truth normal image to calculate the L1 loss for supervised training. It has the same architecture as our SIR model but with only a single prediction head and the forward warping module. Three networks were trained for each distortion model separately. SSL-S has the same architecture as our SIR model but with only a single prediction head and the forward and backward warping module. Intra-model consistency loss is used to train SSL-S in a self-supervised manner. Likewise, three networks were trained for each distortion model separately and used for evaluation. In contrast to SSL-S, SSL-M has the exact same architecture as our SIR model and is trained using the intra-model consistency loss. We test these models on the test sets synthesized using different distortion models. The results are summarized in Table 1. Note that we distinguish the rectification model by the distortion model that is used to synthesize the training set for training that rectification model, as denoted by the second column in Table 1. For SSL-M and SIR with multiple prediction heads, the name in the second column denotes the corresponding head. The name in the first row denotes the corresponding test set.

From Table 1, we have several findings. **First**, FOV and DM generally have a good self-consistency property since the model trained on images synthesized by a specific distortion model performs best on the corresponding test set synthesized by the same distortion model, as shown in the diagonal. ED also has a good self-consistency in most cases except for SSL-S and SIR, where DM outperforms ED. As indicated by the average score across all the test sets, DM generally has the best universality in all the cases except for SSL-M, where DM is only marginally worse than ED. This finding is the same as that in [35]. **Second**, SSL-S achieves comparable performance as SL, which confirms the value of the proposed self-supervised learning idea. Moreover, the universality of DM by SSL-S is even better than that by SL, implying a better generalization ability for deal-

		FOV	DM	ED	Avg.
SL	FOV	24.78/0.82	16.57/0.45	18.67/0.54	20.00/0.60
	DM	20.61/0.62	23.51/0.78	24.64/0.81	22.92/0.74
	ED	18.66/0.55	22.10/0.72	24.72/0.82	21.83/0.70
SSL-S	FOV	24.26/0.80	16.05/0.42	18.14/0.50	19.48/0.57
	DM	21.52/0.67	24.17/0.80	24.51/0.81	23.40/0.76
	ED	21.13/0.67	18.86/0.58	19.26/0.60	19.75/0.62
SSL-M	FOV	23.58/0.78	16.39/0.44	18.74/0.53	19.57/0.58
	DM	21.71/0.69	24.63/0.82	24.77/0.81	23.70/0.77
	ED	22.06/0.69	24.02/0.79	25.48/0.84	23.85/0.77
SIR	FOV	23.43/0.78	16.23/0.44	18.45/0.52	19.37/0.58
	DM	22.92/0.71	24.90/0.83	25.77/0.85	24.53/0.80
	ED	22.74/0.71	24.24/0.80	25.36/0.83	24.11/0.78

Table 1. PSNR and SSIM of different models on the test sets synthesized using different distortion models, *i.e.*, FOV, DM, and ED.

ing with various distortions. **Third**, after employing multiple prediction heads, SSL-M improves the performance further, especially for the ED case, whose universality improves from 19.75dB to 23.85dB. Note that SSL-M did not use the inter-model consistency loss. Thereby, it demonstrates that joint training of multiple heads in a multi-task learning framework is beneficial, probably because a better shared encoder can be learned by exploiting the complementarity between different distortion models. **Fourth**, after exploiting the inter-model consistency, SIR achieves the best universality for DM and ED among all the models and comparable universality for FOV as others, *e.g.*, the universality of DM is further improved to 24.53db (PSNR) and 0.8 (SSIM). These results validate the effectiveness of the proposed self-supervised learning model by exploiting both intra-model and inter-model consistency.

Choice of the Inter-model Loss. As described in Section 3.2, there are different choices of the inter-model loss, *i.e.*, based on $\hat{\mathcal{M}}_1 \sim \hat{\mathcal{M}}_4$. In this part, we evaluate these choices and summarize the results in Table 4. There are several empirical findings. **First**, compared with SSL-M, using the inter-model consistency losses among all the models does not show significant improvement. For example, the universality of FOV and DM improves slightly, *e.g.*, 0.2dB and 0.3dB, while the universality of ED drops by 1.07dB, from 23.85dB to 22.78dB. **Second**, comparing SIR- $\hat{\mathcal{M}}_2$ and SIR- $\hat{\mathcal{M}}_3$ with SSL-M, the universality of DM and ED is not be improved significantly or even becomes worse while the universality of FOV is indeed improved, *e.g.*, from 19.57dB to 19.78dB and 20.05dB, showing that the prediction head of FOV may take advantage of DM and ED from the inter-model consistency. In addition, DM and ED seem to be more consistent with each other than FOV, since the universality of DM and ED by SIR- $\hat{\mathcal{M}}_4$ is better than that of SIR- $\hat{\mathcal{M}}_2$ and SIR- $\hat{\mathcal{M}}_3$. It can also explain why using all inter-model consistency loss in SIR- $\hat{\mathcal{M}}_1$ does not lead to better performance. In conclusion, we choose SIR- $\hat{\mathcal{M}}_4$ as the default setting due to its best average universality.

¹The source code and models will be made publicly available.

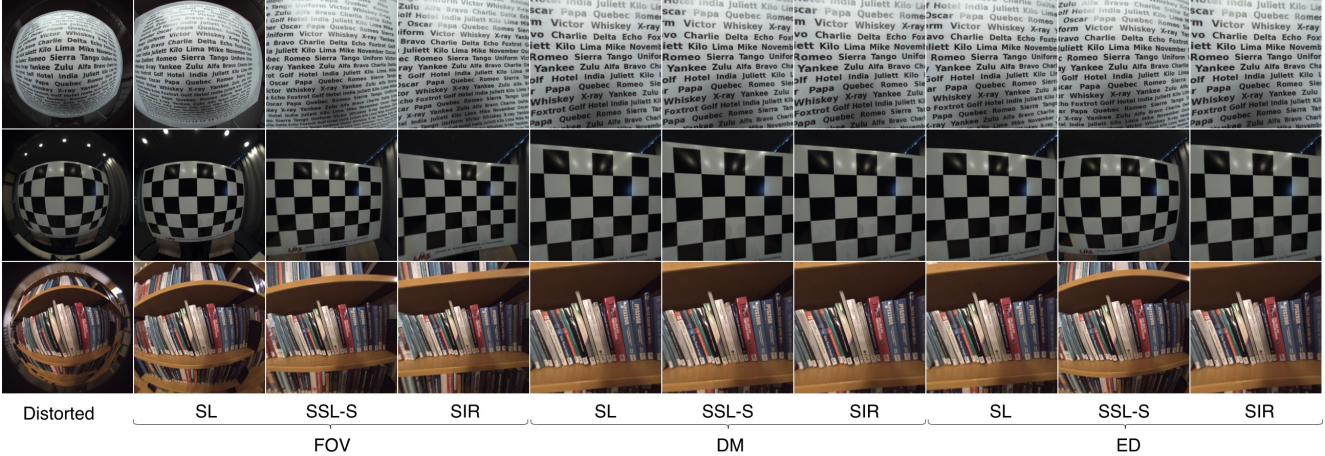


Figure 5. Visual comparison between the supervised baseline and several variants of our SIR model on the real fisheye video dataset [12]. FOV, DM, and ED have the same meaning as those in the second column in Table 1 (Refer to the end of the first paragraph in Section 4.2).

	FOV	DM	ED	Avg.
FOV	24.74/0.82	16.33/0.44	18.24/0.51	19.77/0.59
SIR- $\hat{\mathcal{M}}_1$ DM	22.36/0.69	24.36/0.80	25.29/0.83	24.00/0.77
ED	21.47/0.66	22.64/0.73	24.23/0.79	22.78/0.73
FOV	24.23/0.80	16.58/0.45	18.53/0.52	19.78/0.59
SIR- $\hat{\mathcal{M}}_2$ DM	22.24/0.69	24.35/0.80	24.94/0.82	23.84/0.77
ED	21.82/0.67	23.90/0.78	25.98/0.85	23.90/0.77
FOV	25.54/0.84	16.23/0.43	18.37/0.51	20.05/0.59
SIR- $\hat{\mathcal{M}}_3$ DM	21.54/0.66	24.48/0.81	24.96/0.82	23.66/0.76
ED	20.66/0.63	23.60/0.77	25.39/0.84	23.22/0.75
FOV	23.43/0.78	16.23/0.44	18.45/0.52	19.37/0.58
SIR- $\hat{\mathcal{M}}_4$ DM	22.92/0.71	24.90/0.83	25.77/0.85	24.53/0.80
ED	22.74/0.71	24.24/0.80	25.36/0.83	24.11/0.78

Table 2. PSNR and SSIM of the ablation study on the choice of inter-model consistency loss. For $\hat{\mathcal{M}}_i$, please refer to Section 3.2.

We present some visual results obtained by the supervised learning baseline and different variants of our SIR model in Figure 5. The test images are from the real fisheye video dataset [12]. **First**, SL and SSL-S trained on the images synthesized based on FOV have limited ability for image rectification, although SSL-S performs a little better than SL as shown in the second and third column. It is consistent with the object metrics in Table 1 that FOV has the worst universality. Nevertheless, our SIR model performs much better than SL and SSL-S, *i.e.*, the distortion can be corrected to a great extent as shown in the fourth column, demonstrating that the proposed self-supervised learning model based on both intra-model and inter-model consistency can improve the universality of FOV significantly. **Second**, in the case of DM, all the three models achieve comparable performance and can correct the distortion successfully. Together with the results of objective metrics, we can conclude that the DM distortion model has the best representation ability to account for different distortion types

than others (*i.e.*, best universality). **Third**, in the case of ED, the visual results are also consistent with those in Table 1 that SSL-S performs worst. In general, our SIR model has the best generalization performance on real images.

4.3. Comparison with Representative Methods

Method	PSNR	SSIM
Alemán-Flores [1]	12.87	0.32
Rong [29]	17.52	0.55
Xue [38]	27.61	0.87
Ours SIR	25.98	0.85

Table 3. PSNR and SSIM of SIR and representative methods.

Since many methods are not open-sourced or hard to train to reproduce the results, we compared our SIR methods with a traditional method proposed by Alemán-Flores *et al.* in [1] and two deep learning methods proposed by Rong [29] and Xue [38]. Rong’s method classifies distortion parameters into 401 categories via a deep neural network and obtains the predicted parameter by weighted average during inference. Xue’s method is the state-of-the-art, which first trains a line detection module using extra line annotations and then trains a rectification module to regress the distortion parameter by emphasizing the re-projection loss of lines. They are the representative traditional-based method, the deep learning-based method using ground-truth labels, and the deep learning-based method using extra annotations. We re-implemented Rong’s method by increasing the number of categories from 10 to 401 progressively and fine-tuned the model stage-by-stage. In this way, it converges faster and performs slightly better. Their results of PSNR and SSIM are summarized in Table 3. As can be seen, our SIR outperforms Alemán-Flores’s method and Rong’s method by a large margin. It is comparable with

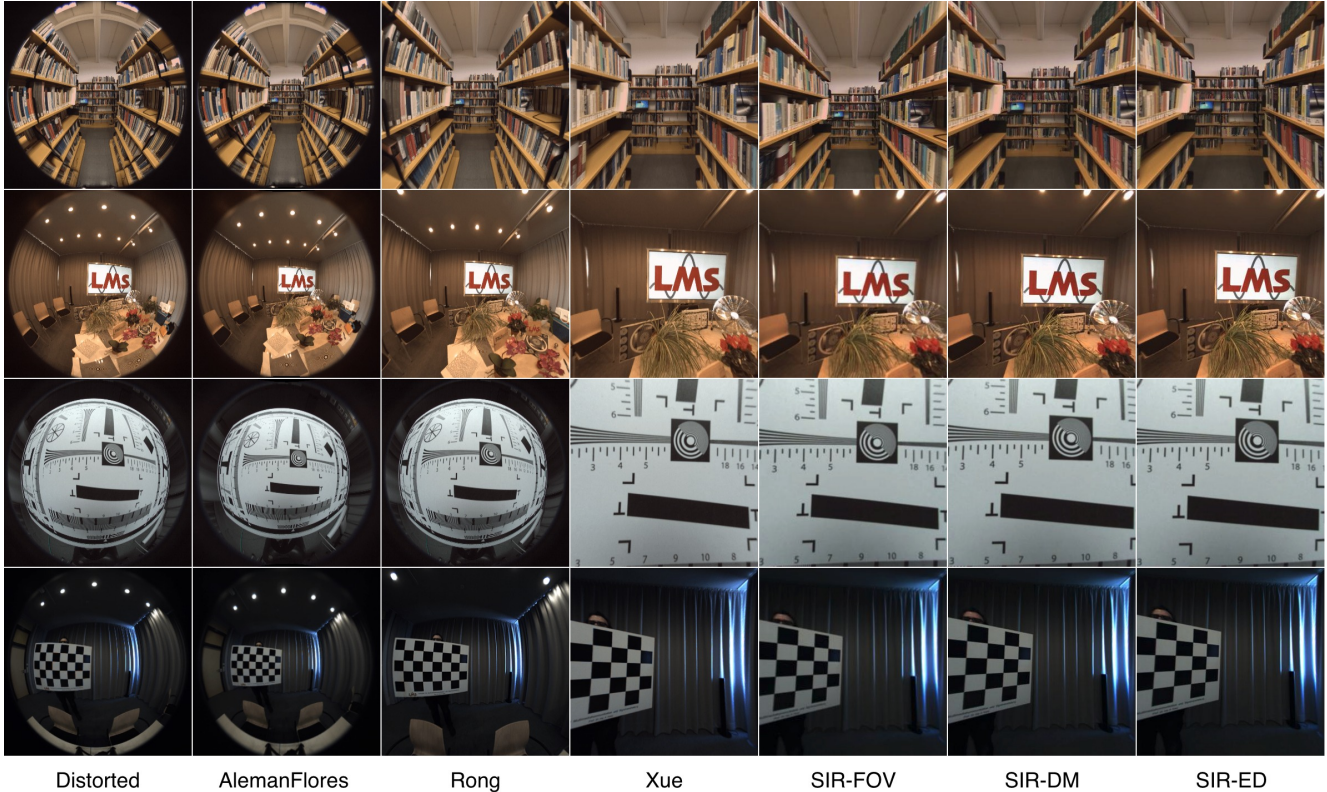


Figure 6. Visual comparison between SIR and several representative methods including Alemán-Flores [1], Rong [29], and Xue [38], on the real fisheye video dataset [12]. FOV, DM, and ED denote the corresponding prediction head in our SIR model.

Xue’s method which leverages lines to regularize the rectification process. Note that SIR does not need any annotations, thereby it has great potential in practical applications.

We also compared SIR with these methods on real fish-eye images as shown in Figure 6. As can be seen, the traditional method has a limited image rectification ability on real fisheye images. Rong’s method can correct the distortion to some extent, though not very pleasing. Xue’s method achieves the best performance among them, which can successfully recover the normal image. Our method achieves comparable results with Xue’s method no matter which prediction head is used, *e.g.*, straight lines and upright rectangles. The results validate that our self-supervised method can efficiently leverage the intra-model and inter-model consistency and improve the universality of all the distortion models, leading to a strong generalization ability.

4.4. Limitation Discussion and Future Work

The proposed self-supervised method shows promising results on both synthesized distorted images and real fish-eye images. Nevertheless, there is still room for further improvement. First, we only choose three typical distortion models in this paper which have analytical forward and backward warping functions. Other distortion models with

the same property can be explored in our method. Besides, for models only having an analytical warping function in one direction, *i.e.*, forward or backward, our method can be extended further to be compatible with them by predicting the warping field instead of distortion parameter. On the other hand, although we only use synthetic images for training, our method has the potential to use unlabeled real distorted images for training, which can be captured by either changing lenses or parameters such as focal length.

5. Conclusion

In this paper, we proposed the self-supervised learning idea for image rectification by exploiting intra-model and inter-model consistency. With a shared encoder and multiple prediction heads, our model can learn better an encoding feature representation via the complementary back-propagate signals from different heads. Both kinds of consistency improve the universality of all the three distortion models, leading to a model with better generalization ability on real fisheye images. The proposed self-supervised learning method is scalable and flexible that can be improved further by involving more distortion models with/without analytical forward and backward warping functions.

References

- [1] Miguel Alemán-Flores, Luis Alvarez, Luis Gomez, and Daniel Santana-Cedr s. Automatic Lens Distortion Correction Using One-Parameter Division Models. *Image Processing On Line*, 4:327–343, 2014. 1, 4, 5, 7, 8, 11, 14
- [2] Michel Antunes, Joao P. Barreto, Djamilia Aouada, and Bjorn Ottersten. Unsupervised Vanishing Point Detection and Camera Calibration from a Single Manhattan Image with Radial Distortion. In *Proceedings of IEEE Conference on Computer Vision and Pattern Recognition*, pages 6691–6699, 2017. 1
- [3] J.P. Barreto and K. Daniilidis. Fundamental matrix for cameras with radial distortion. In *Proceedings of IEEE International Conference on Computer Vision Systems*, pages 625–632 Vol. 1, 2005. 2
- [4] Oleksandr Bogdan, Viktor Eckstein, Francois Rameau, and Jean-Charles Bazin. DeepCalib: A deep learning approach for automatic intrinsic calibration of wide field-of-view cameras. In *ACM SIGGRAPH*, 2018. 2, 3
- [5] Faisal Bukhari and Matthew N. Dailey. Robust Radial Distortion from a Single Image. In *Advances in Visual Computing*, volume 6454, pages 11–20, 2010. 1
- [6] Faisal Bukhari and Matthew N. Dailey. Automatic Radial Distortion Estimation from a Single Image. *Journal of Mathematical Imaging and Vision*, 45(1):31–45, Jan. 2013. 5
- [7] Robert Carroll, Maneesh Agrawal, and Aseem Agarwala. Optimizing content-preserving projections for wide-angle images. In *ACM SIGGRAPH*, 2009. 2
- [8] David Caruso, Jakob Engel, and Daniel Cremers. Large-scale direct SLAM for omnidirectional cameras. In *Proceedings of IEEE International Conference on Intelligent Robots and Systems*, pages 141–148, 2015. 1
- [9] Chun-Hao Chao, Pin-Lun Hsu, Hung-Yi Lee, and Yu-Chiang Frank Wang. Self-Supervised Deep Learning for Fisheye Image Rectification. In *Proceedings of IEEE International Conference on Acoustics, Speech and Signal Processing*, pages 2248–2252, 2020. 3
- [10] Ting Chen, Simon Kornblith, Mohammad Norouzi, and Geoffrey Hinton. A simple framework for contrastive learning of visual representations. *arXiv preprint arXiv:2002.05709*, 2020. 3
- [11] Jia Deng, Wei Dong, Richard Socher, Li-Jia Li, Kai Li, and Li Fei-Fei. ImageNet: A large-scale hierarchical image database. In *Proceedings of IEEE Conference on Computer Vision and Pattern Recognition*, pages 248–255, 2009. 6
- [12] Andrea Eichenseer and Andre Kaup. A data set providing synthetic and real-world fisheye video sequences. In *Proceedings of IEEE International Conference on Acoustics, Speech and Signal Processing*, pages 1541–1545, 2016. 7, 8, 11, 13
- [13] A.W. Fitzgibbon. Simultaneous linear estimation of multiple view geometry and lens distortion. In *Proceedings of IEEE Conference on Computer Vision and Pattern Recognition*, volume 1, pages I–125–I–132, 2001. 2, 3
- [14] Kaiming He, Xiangyu Zhang, Shaoqing Ren, and Jian Sun. Deep Residual Learning for Image Recognition. In *Proceedings of IEEE Conference on Computer Vision and Pattern Recognition*, pages 770–778, 2016. 3
- [15] Ciaran Hughes, Patrick Denny, Martin Glavin, and Edward Jones. Equidistant Fish-Eye Calibration and Rectification by Vanishing Point Extraction. *IEEE Transactions on Pattern Analysis and Machine Intelligence*, 32(12):2289–2296, Dec. 2010. 3
- [16] Longlong Jing and Yingli Tian. Self-supervised Visual Feature Learning with Deep Neural Networks: A Survey. *IEEE Transactions on Pattern Analysis and Machine Intelligence*, pages 1–1, 2020. 3
- [17] Longlong Jing and Yingli Tian. Self-supervised visual feature learning with deep neural networks: A survey. *IEEE Transactions on Pattern Analysis and Machine Intelligence*, 2020. 3
- [18] Yeong Won Kim, Chang-Ryeol Lee, Dae-Yong Cho, Yong Hoon Kwon, Hyeok-Jae Choi, and Kuk-Jin Yoon. Automatic content-aware projection for 360 videos. In *Proceedings of IEEE International Conference on Computer Vision*, pages 4753–4761, 2017. 2
- [19] Hongdong Li and Richard Hartley. A non-iterative method for correcting lens distortion from nine-point correspondences. In *Proceedings of IEEE International Conference on Computer Vision Workshops*, 2005. 2
- [20] Xiaoyu Li, Bo Zhang, Pedro V. Sander, and Jing Liao. Blind Geometric Distortion Correction on Images Through Deep Learning. In *Proceedings of IEEE Conference on Computer Vision and Pattern Recognition*, pages 4850–4859, 2019. 1, 2, 3
- [21] Kang Liao, Chunyu Lin, Yao Zhao, and Moncef Gabbouj. DR-GAN: Automatic Radial Distortion Rectification Using Conditional GAN in Real-Time. *IEEE Transactions on Circuits and Systems for Video Technology*, 30(3):725–733, 2020. 1, 3
- [22] Kang Liao, Chunyu Lin, Yao Zhao, and Mai Xu. Model-Free Distortion Rectification Framework Bridged by Distortion Distribution Map. *IEEE Transactions on Image Processing*, 29:3707–3718, 2020. 2, 3
- [23] Manuel Lopez, Roger Mari, Pau Gargallo, Yubin Kuang, Javier Gonzalez-Jimenez, and Gloria Haro. Deep Single Image Camera Calibration With Radial Distortion. In *Proceedings of IEEE Conference on Computer Vision and Pattern Recognition*, pages 11809–11817, 2019. 2, 3
- [24] Ivan Markovic, Francois Chaumette, and Ivan Petrovic. Moving object detection, tracking and following using an omnidirectional camera on a mobile robot. In *Proceedings of IEEE International Conference on Robotics and Automation*, pages 5630–5635, 2014. 1
- [25] R. Melo, M. Antunes, J.P. Barreto, G. Falcao, and N. Goncalves. Unsupervised Intrinsic Calibration from a Single Frame Using a ‘Plumb-Line’ Approach. In *Proceedings of IEEE International Conference on Computer Vision Systems*, pages 537–544, 2013. 2
- [26] Ishan Misra and Laurens van der Maaten. Self-supervised learning of pretext-invariant representations. In *Proceedings of IEEE Conference on Computer Vision and Pattern Recognition*, June 2020. 3
- [27] James Pritts, Zuzana Kukelova, Viktor Larsson, Yaroslava Lochman, and Ondrej Chum. Minimal Solvers for Rectifying from Radially-Distorted Scales and Change of Scales. *International Journal of Computer Vision*, 128(4):950–968, 2020. 1

- [28] Alejandro Rituerto, Luis Puig, and J.J. Guerrero. Visual SLAM with an Omnidirectional Camera. In *Proceedings of IEEE International Conference on Pattern Recognition*, pages 348–351, 2010. [1](#)
- [29] Jiangpeng Rong, Shiyao Huang, Zeyu Shang, and Xianghua Ying. Radial Lens Distortion Correction Using Convolutional Neural Networks Trained with Synthesized Images. In *Proceedings of the Asian Conference on Computer Vision*, volume 10113, pages 35–49, 2016. [1](#), [2](#), [3](#), [4](#), [5](#), [7](#), [8](#), [14](#)
- [30] Yongjie Shi, Danfeng Zhang, Jingsi Wen, Xin Tong, Xi-anhua Ying, and Hongbin Zha. Radial Lens Distortion Correction by Adding a Weight Layer with Inverted Foveal Models to Convolutional Neural Networks. In *Proceedings of IEEE International Conference on Pattern Recognition*, pages 1–6, 2018. [2](#), [3](#), [4](#)
- [31] YiChang Shih, Wei-Sheng Lai, and Chia-Kai Liang. Distortion-free wide-angle portraits on camera phones. *ACM Transactions on Graphics*, 38(4):1–12, 2019. [2](#)
- [32] R. Matt Steele and Christopher Jaynes. Overconstrained Linear Estimation of Radial Distortion and Multi-view Geometry. In *Proceedings of the European Conference on Computer Vision*, volume 3951, pages 253–264, 2006. [2](#)
- [33] P. Sturm. Multi-View Geometry for General Camera Models. In *Proceedings of IEEE Conference on Computer Vision and Pattern Recognition*, volume 1, pages 206–212, 2005. [2](#)
- [34] Peter Sturm. Camera Models and Fundamental Concepts Used in Geometric Computer Vision. *Foundations and Trends in Computer Graphics and Vision*, 6(1-2):1–183, 2010. [4](#)
- [35] Zhongwei Tang, Rafael Grompone Von Gioi, Pascal Monasse, and Jean-Michel Morel. Self-consistency and universality of camera lens distortion models, 2012. [2](#), [6](#)
- [36] Zhongwei Tang, Rafael Grompone von Gioi, Pascal Monasse, and Jean-Michel Morel. A Precision Analysis of Camera Distortion Models. *IEEE Transactions on Image Processing*, 26(6):2694–2704, June 2017. [3](#), [4](#)
- [37] Jin Wei, Chen-Feng Li, Shi-Min Hu, Ralph R. Martin, and Chiew-Lan Tai. Fisheye Video Correction. *IEEE Transactions on Visualization and Computer Graphics*, 18(10):1771–1783, 2012. [2](#)
- [38] Zhucun Xue, Nan Xue, Gui-Song Xia, and Weiming Shen. Learning to Calibrate Straight Lines for Fisheye Image Rectification. In *Proceedings of IEEE Conference on Computer Vision and Pattern Recognition*, pages 1643–1651, 2019. [1](#), [2](#), [3](#), [5](#), [7](#), [8](#)
- [39] Zhu-Cun Xue, Nan Xue, and Gui-Song Xia. Fish-eye Distortion Rectification from Deep Straight Lines. *arXiv:2003.11386 [cs]*, 2020. [1](#)
- [40] Xiaoqing Yin, Xinchao Wang, Jun Yu, Maojun Zhang, Pascal Fua, and Dacheng Tao. FishEyeRecNet: A Multi-context Collaborative Deep Network for Fisheye Image Rectification. In *Proceedings of the European Conference on Computer Vision*, volume 11214, pages 475–490, 2018. [1](#), [2](#), [3](#), [5](#)
- [41] Mi Zhang, Jian Yao, Menghan Xia, Kai Li, Yi Zhang, and Yaping Liu. Line-based Multi-Label Energy Optimization for fisheye image rectification and calibration. In *Proceedings of IEEE Conference on Computer Vision and Pattern Recognition*, pages 4137–4145, 2015. [1](#), [2](#)
- [42] Bolei Zhou, Hang Zhao, Xavier Puig, Tete Xiao, Sanja Fidler, Adela Barriuso, and Antonio Torralba. Semantic Understanding of Scenes Through the ADE20K Dataset. *International Journal of Computer Vision*, 127(3):302–321, 2019. [2](#), [5](#), [11](#), [12](#)

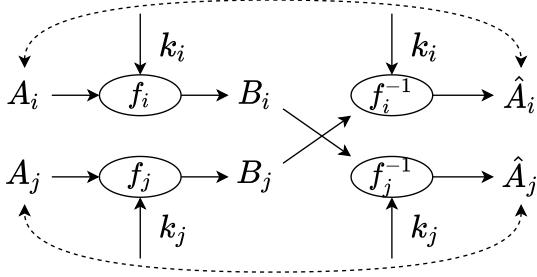


Figure 7. Illustration of the intra-model loss that works across different models, *i.e.* L_r . A_i and A_j are two distorted images from the i th and j th distortion models. B_i and B_j are the rectified ones in i th and j th heads, respectively. B_i and B_j are re-distorted using the backward warping module from the other head, generating \hat{A}_j and \hat{A}_i .

Appendices

A. Overview

This document provides more experiments, test results, and information to the main paper. In Section B, we provide more ablation studies on the inter-model loss. More visual results are given in Section C both on the synthesized dataset [42] and the real fisheye video dataset [12]. Finally, the runtime and model size of our method are

B. More Experiments

The proposed intra-model consistent loss (denoted as L_{intra}) works on the distorted and re-distorted images in the same head, which means they are under the same distortion model. Here, we provide the test results when the intra-model loss is calculated between the distorted and re-distorted ones from different heads. The rectified images are re-distorted using the backward warping module in another head, as shown in Figure 7. Technically, it is not an intra-model loss anymore. It is an inter-model re-projection loss. The experiment using this kind of re-projection loss is denoted as L_r .

Similarly, the proposed inter-model consistent loss (denoted as L_{inter}) only works on the images that are rectified by the head under the same distortion model as the one used to synthesize the input images. Here, we provide the test results when the inter-model loss is added on all images both from the same head (denoted as L_s) and from different heads (denoted as L_c). The former one means that the rectified results of distorted images under different models in one specific head (*i.e.* using one specific distortion model) should be consistent. And the latter one says the rectified outputs of different heads should be the same. To be more specific, we take FOV, DM, and ED models in the main paper as examples. The difference between L_s , L_c and the

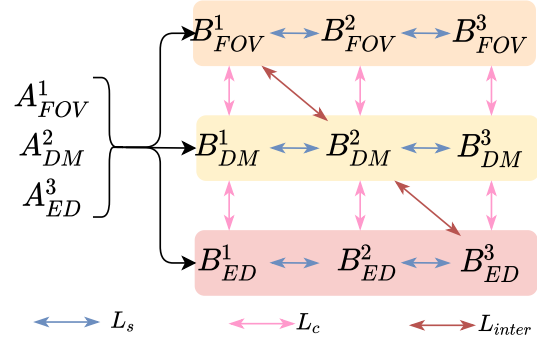


Figure 8. The difference between L_s , L_c and L_{inter} .

proposed L_{inter} is illustrated in Figure 8. Given three images A_{FOV}^1 , A_{DM}^2 , A_{ED}^3 from FOV, DM and ED distortion model, the rectified images in each head are B_i^1 , B_i^2 , B_i^3 ($i \in \{FOV, DM, ED\}$) respectively, *e.g.* B_{FOV}^3 is the rectified result of A_{ED}^3 in FOV head. L_s adds regulation on the results in each head, *e.g.* B_{FOV}^1 , B_{FOV}^2 , B_{FOV}^3 in FOV head, while L_c adds regulation between the results of every two heads, *e.g.* (B_{FOV}^1 , B_{FOV}^2 , B_{FOV}^3) and (B_{DM}^1 , B_{DM}^2 , B_{DM}^3) from FOV and DM heads. Our proposed inter-model loss only works on the diagonal results, which are the rectified results of input images having the same distortion model as that in the head, *e.g.* B_{FOV}^1 in FOV head for A_{FOV}^1 , B_{DM}^2 in DM head for A_{DM}^2 , and B_{ED}^3 in ED head for A_{ED}^3 .

The test results are listed in Table 4. When L_s and L_r work alone, they fail to rectify the input distorted images since the images collapse to some common distorted states that all images could be transformed to. The rectified results are still distorted when the loss is minimized. If L_c is used, the common state could be closer to the correct one and higher PSNR and SSIM are achieved. When L_s and L_r work with L_c , PSNR and SSIM do not be improved. On the contrary, negative effects are observed. Especially, when L_s works with L_c which is equivalent to regular all the rectified outputs of all input images from all heads, it gives the worst objective metrics. With the proposed L_{intra} only, we can get superior performance. And together with L_{inter} the highest overall PSNR and SSIM are achieved.

C. Additional Visual Results

More test results on the synthesized test dataset and real fisyeve video dataset [12] are provided in Figure 9 and Figure 10. SL, SSL-S and SIR have the same meaning as in main paper.

D. Running Time

We compare the running time of our method with those of the representative traditional method [1] and the pa-



Figure 9. Comparison of the visual results with the baseline methods on synthesized test dataset. The first column is the synthesized distorted image. *realB* is the original normal image from the ADE20K test dataset [42].



Figure 10. Comparison of the visual results with the baseline methods on fisheye video dataset [12]. The first column contains the input real fisheye images.

		FOV	DM	ED	Avg.
L_s	FOV	NA	NA	NA	NA
	DM	NA	NA	NA	NA
	ED	NA	NA	NA	NA
L_r	FOV	NA	NA	NA	NA
	DM	NA	NA	NA	NA
	ED	NA	NA	NA	NA
L_c	FOV	21.80/0.71	16.46/0.47	18.25/0.52	18.84/0.57
	DM	20.68/0.66	21.50/0.68	21.27/0.67	21.15/0.67
	ED	21.09/0.67	21.65/0.68	21.37/0.67	21.37/0.67
$L_s + L_c$	FOV	11.75/0.38	11.34/0.37	11.59/0.38	11.56/0.38
	DM	13.52/0.42	13.68/0.44	13.65/0.44	13.62/0.43
	ED	13.51/0.43	13.66/0.44	13.64/0.44	13.60/0.44
$L_r + L_c$	FOV	20.82/0.68	16.42/0.46	17.69/0.50	18.31/0.55
	DM	20.31/0.65	20.14/0.62	19.73/0.61	19.94/0.63
	ED	20.87/0.67	20.02/0.61	19.69/0.60	20.19/0.63
$L_s + L_r + L_c$	FOV	20.50/0.66	16.32/0.45	17.45/0.50	18.09/0.54
	DM	20.39/0.65	19.67/0.60	19.22/0.59	19.76/0.61
	ED	20.66/0.66	19.42/0.59	19.15/0.59	19.74/0.61
L_{intra}	FOV	23.58/0.78	16.39/0.44	18.74/0.53	19.57/0.58
	DM	21.71/0.69	24.63/0.82	24.77/0.81	23.70/0.77
	ED	22.06/0.69	24.02/0.79	25.48/0.84	23.85/0.77
$L_{intra} + L_{inter}$	FOV	23.43/0.78	16.23/0.44	18.45/0.52	19.37/0.58
	DM	22.92/0.71	24.90/0.83	25.77/0.85	24.53/0.80
	ED	22.74/0.71	24.24/0.80	25.36/0.83	24.11/0.78

Table 4. More ablation studies on the inter-model loss using PSNR and SSIM. NA means the experiment fails and images can not be rectified. The setting of each experiment can be found in Section B.

parameter regression method proposed in [29]. We test the images on NVIDIA Tesla V100 GPU with input size 257×257 . Generally, traditional methods are slower than deep learning-based methods since the latter normally only need a forward pass to predict the parameters, while the former has to estimate the parameters via a time-consuming optimization procedure. Although our method is slower than Rong *et al.* [29], it can still run in real-time (> 60 FPS) even with three rectification heads.

Methods	Time
Alemán-Flores [1]	1.301
Rong [29]	0.003
w/ one head	0.009
Ours w/ two heads	0.012
w/ three heads	0.015

Table 5. Comparison of running time (seconds).